The transition probabilities from the ground state to the excited J = 0 u + 1 levels of H2: Measurements and ab initio quantum defect study

M. Glass-Maujean, Ch. Jungen, H. Schmoranzer, I. Haar, A. Knie, P. Reiss, and A. Ehresmann

Citation: The Journal of Chemical Physics **135**, 144302 (2011); doi: 10.1063/1.3646734
View online: http://dx.doi.org/10.1063/1.3646734
View Table of Contents: http://scitation.aip.org/content/aip/journal/jcp/135/14?ver=pdfcov
Published by the AIP Publishing

The transition probabilities from the ground state to the excited $J = 0$ $^1\Sigma_u^+$ levels of H_2: Measurements and *ab initio* quantum defect study

M. Glass-Maujean,[1] Ch. Jungen,[2,3,a)] H. Schmoranzer,[4] I. Haar,[5] A. Knie,[5] P. Reiss,[5] and A. Ehresmann[5]

[1]*Laboratoire de Physique Moléculaire pour l'Atmosphère et l'Astrophysique, Université Pierre et Marie Curie, 4 place Jussieu, 75252 Paris Cedex 05, France*
[2]*Laboratoire Aimé Cotton du CNRS, Bâtiment 505, Université de Paris-Sud, F-91405 Orsay, France*
[3]*Department of Physics and Astronomy, University College London, London WC1E 6BT, United Kingdom*
[4]*Fachbereich Physik, Technische Universität Kaiserslautern, D-67653 Kaiserslautern, Germany*
[5]*Institute of Physics and Interdisciplinary Nanostructure, Science and Technology, Heinrich-Plett-Str. 40, Universität Kassel, D-34132 Kassel, Germany*

(Received 5 July 2011; accepted 16 September 2011; published online 10 October 2011)

The energies, widths and absolute intensities of the P(1) $v'' = 0$, $J'' = 1$ absorption transitions of H_2 have been measured in the spectral range of 81-75 nm using monochromatized synchrotron radiation. This work completes and extends previous observations, in particular those of Herzberg and Jungen [J. Mol. Spectrosc. **41**, 425 (1972)]. *Ab initio* multichannel quantum defect theory (MQDT) is used to corroborate the spectral analysis of the experimental data. Line intensities and decay widths are also calculated using MQDT. © *2011 American Institute of Physics*. [doi:10.1063/1.3646734]

I. INTRODUCTION

The emission of radiation by molecular hydrogen H_2 is known to be an important astrophysical process. Since the Voyager and International Ultraviolet Explorer flights and, more recently, since the Hubble Space Telescope and the Galileo space craft have become operational, it has been established that H_2 emission is the primary vacuum ultraviolet (VUV) and EUV emission process in the atmospheres of outer planets.[1,2] The determination of energies and transition probabilities of molecular transitions is of crucial importance for astrophysical studies since it enables the computation of simulated molecular spectra to be carried out.[3] The experimental study of the emission and absorption spectra of H_2, the smallest neutral molecule, is also of interest in itself, and in the past has triggered advances of molecular theory and modelling.[4–6]

The absorption spectrum of H_2 in the range of 85–72 nm is a complex many-line spectrum because numerous Rydberg series converging toward various vibration-rotation levels of the H_2^+ ion appear superimposed and interleaved. They mutually interact through non-adiabatic coupling which disrupts the regular pattern of the H atom-like Rydberg series.[5] The effects of these couplings are not uniformly distributed among the various quantum states, but depend in a characteristic manner on the rotational quantum number and/or parity of the excited state levels considered. The present paper deals with the $J = 0$ *ungerade* singlet excited levels of H_2 which have positive total parity. These are excited in photoabsorption via the P(1) optical transitions originating from the $v'' = 0$, J'' $= 1$ level in the ground state. The upper states of these transitions have pure $^1\Sigma_u^+$ electronic symmetry and may interact via $\Sigma \sim \Sigma$ vibronic interaction with all other $^1\Sigma_u^+$, $J = 0$ levels of the molecule. Rotational-electronic $\Sigma \sim \Pi$ non-adiabatic coupling on the other hand does not affect these levels. Singlet-triplet interactions due to spin-orbit or hyperfine interaction are very weak in H_2, too weak to be detected in the present experiment. They are therefore not included in the present analysis.

The present work is a part of an effort to provide a coherent and systematic experimental and theoretical account of the absorption spectrum of diatomic hydrogen and its isotopomers up to the H($1s$)+H($n = 3$) dissociation limit. In several previous papers[7–9] we have investigated the manifold of excited singlet *ungerade* J levels corresponding to $J \geq 1$ and total parity $-(-1)^J$. These levels have pure $^1\Pi_u^-$ electronic symmetry and, like the levels studied in the present paper, are not subject to rotational-electronic non-adiabatic coupling. They undergo $\Pi \sim \Pi$ vibronic interactions with levels of the same electronic symmetry (as well as J and parity). In that case we found that the energies were only little perturbed by the vibronic interactions – as had in fact been recognized previously[5,10] – but that the line intensities exhibit strong perturbations even in cases where the level positions are not noticeably perturbed by the vibronic interaction. It is known[5,10] that the vibronic interactions affecting the $^1\Sigma_u^+$, $J = 0$ levels of H_2 are intrinsically far stronger than those affecting the $^1\Pi_u^-$, $J \geq 1$ levels. The strength of vibronic coupling is directly related to the way the $p\lambda$ Rydberg orbital is oriented with respect to the nuclear framework: the Σ states correspond to a $p\sigma_u$ Rydberg electron orbital lying along the molecular axis, whereas the Π states correspond to a $p\pi_u$ Rydberg electron orbital oriented perpendicular to the axis. The nuclear and electronic motions are therefore more intimately coupled in the first as compared to the second situation.

Previous measurements of H_2 line frequencies in the VUV region include the work of Herzberg and Jungen[5]

a)Author to whom correspondence should be addressed. Electronic mail: christian.jungen@lac.u-psud.fr.

(down to 78 nm) and of Dehmer and Chupka[11] (down to 75 nm). These spectra were obtained at low temperature (78 K). We have previously studied the $B''\bar{B}\,^1\Sigma_u^+ - X\,^1\Sigma_g^+$, $v''=0$,[12] the $np\pi\,^1\Pi_u^- - X\,^1\Sigma_g^+$, $v''=0$,[13] the $5p\sigma\,^1\Sigma_u^+ - X\,^1\Sigma_g^+$, $v''=0$,[14] and the $D'^1\Pi_u - X\,^1\Sigma_g^+$, $v''=0$ (Ref. 15) band systems. In all these studies, absolute line intensities were measured and compared with first principles theoretical calculations, carried out for the most part in the adiabatic approximation.

The present paper, in addition to reporting measurements obtained with higher resolution and greater accuracy than those reported in Refs. 7 and 12–15, contains a fully *ab initio* non-adiabatic multichannel quantum defect (MQDT) analysis of the P(1) line positions, intensities, and widths, based on the latest quantum-chemical clamped-nuclei calculations of Wolniewicz and collaborators.[16,17]

II. EXPERIMENT

The experimental set-up has been described in detail in previous publications.[8,9] The intensities of the absorption spectrum, recorded under high spectral resolution, have been calibrated directly, based on the known gas pressure and the absorption path length. Simultaneously, the photoionization and photodissociation excitation spectra were recorded. The VUV photons coming from the undulator beamline U125/2-10m-NIM of BESSY II were dispersed by a 10 m-normal-incidence monochromator equipped with a 4800-lines/mm grating giving a spectral resolution of 0.0010 nm in first order[18] (this value represents the convolution of the apparatus function with the Doppler width at room temperature). The uncertainty of the energies of the measured spectra has thus been improved significantly since the earlier publications[7,12–15] and is typically ± 1.0 to ± 1.5 cm^{-1}.

The monochromatized photons were focused into a differentially pumped gas cell of 39 mm length containing H_2 at a pressure of 20 mTorr (26.7 μbar) measured by a baratron gauge. The transmitted light intensity needed for determining the absorption cross section was detected by a photodiode located at the back of the cell. Molecular visible fluorescence and Lyman-α fluorescence radiation from the H($n=2$) atomic fragments were detected simultaneously with the transmitted light. In addition, photoions were collected by applying a voltage of 10 V to one of two electrodes in the target cell. The calibration of the spectra and the measurement procedures have been described in more detail previously.[9,12]

III. THEORETICAL APPROACH

Multichannel quantum defect theory (MQDT) combined with the frame transformation concept is a theoretical approach which is adapted to the description beyond the Born-Oppenheimer approximation of electronically excited molecular systems.[6,19] It surpasses the traditional coupled equations approach in that it is not restricted to just a few excited states of a molecule, but is capable of describing highly excited levels and their dynamics up to the ionization threshold and beyond. Furthermore, using the powerful concept of frame transformations, MQDT bypasses the evaluation of the electronic coupling matrix elements requiring the knowledge of numerical *ab initio* electronic wave functions. This is possible, basically, because MQDT produces explicit electronic wavefunctions for electron radii of the excited electron outside the core, in addition to vibrational-rotational wavefunctions. This is not the case in the traditional coupled-equations approach where only matrix elements involving the electron wavefunctions are considered explicitly. We follow the approach pioneered initially in Ref. 10 and employed and refined recently in Ref. 7.

A. Determination of quantum defects and channel transition moments from quantum-chemical data

We employ here quantum defect theory in its simplest form, in which channel interactions between singly excited and doubly (core) excited Rydberg channels are not included explicitly and ℓ-mixing (coupling between different partial waves), induced by the deviation of the molecular ion core from spherical symmetry, is also not included explicitly. However, as discussed in more detail below, these effects are taken into account in an effective manner since we derive the quantum defects from state-of-the-art *ab initio* quantum chemical calculations which fully account for the physics of the clamped-nuclei molecule.

Specifically, we derive R- and energy- dependent quantum defects from the best available *ab initio* $^1\Sigma_u^+$ potential energy curves, calculated by Wolniewicz and his group,[16] by using the familiar one-channel Rydberg equation

$$U_{np\sigma\,^1\Sigma_u^+}(R) = U^+(R) - \frac{1}{2[n-\mu_{np\sigma\,^1\Sigma_u^+}(R)]^2}, \qquad (1)$$

written here in atomic units. Equation (1) serves to extract $^1\Sigma_u^+$ symmetry clamped-nuclei quantum defects $\mu_{np\sigma\,^1\Sigma_u^+}(R)$ from a set of selected *ab initio* potential energy curves $U_{np\sigma\,^1\Sigma_u^+}(R)$ from Ref. 16. $U^+(R)$ is the $H_2^+\ ^2\Sigma_g^+$ ion core ground state potential energy curve. The labels $np\sigma$ denote the united-atom Rydberg character of the excited orbitals. We use the curves corresponding to $n=3$, 4 and 5 (cf. Fig. 1(a)). These correspond, respectively, in the usual spectroscopic notation to the states B', $B''\bar{B}$, and $5p\sigma$,[20] and in the notation adopted by Wolniewicz to $B3$, $B4$, and $B6$.[16] (For the sake of completeness we mention that according to the notation introduced by Dieke and Crosswhite[21] in their well-known book, the same states would be denoted as $3B$, $4B$, and $5B$, respectively.)

We have not used the $B\,^1\Sigma_u^+$ ($B2$) state in our analysis despite the fact that for small R it represents the $n=2$ member of the $np\sigma$ Rydberg series. This state lies for the most part far below the energy region on which we focus here. In addition, beyond $R \approx 3$ bohrs this state acquires a predominantly ionic ($H^+ + H^-$) non-Rydberg character. A complication arises also in the $B''\bar{B}$ state which we do include in the analysis: for small R this state corresponds to the $4p\sigma$ Rydberg state, but at longer range ($R > 6$ bohrs) it undergoes ℓ-mixing ($p \sim f$) and eventually evolves into a non-Rydberg state with partial ionic character. A second potential minimum occurs, so that

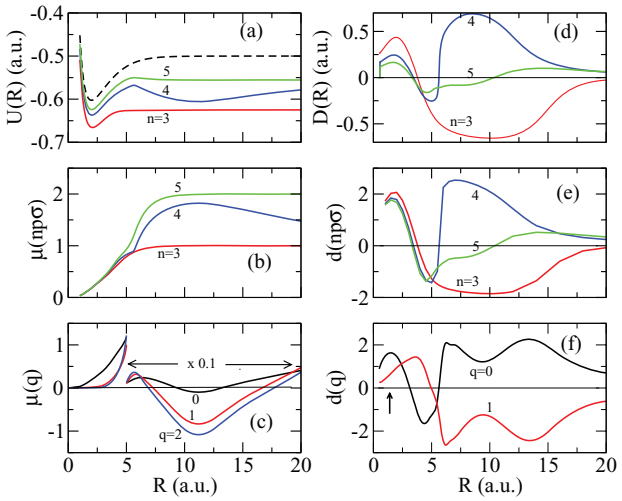

FIG. 1. Reduction of quantum-chemical data to channel parameters adapted for MQDT (H_2, $^1\Sigma_u^+$ symmetry). (a) *Ab initio* potential energy curves $U_{np\sigma\,^1\Sigma_u^+}(R)$ corresponding to the $B3$, $B4$, and $B6$ states (Ref. 16): $n = 3$, red line. $n = 4$, blue line. $n = 5$, green line. Black dashed line: ion core curve $U^+(R)$. (b) Quantum defects extracted from the potential curves by use of Eq. (1) (same symbols as in panel (a)). (c) Quantum defect functions $\mu^{(q)}(R)$ (cf. Eq. (2)): $\mu^{(0)}(R)$ (black line). $0.1 \times \mu^{(1)}(R)$ (red line). $0.01 \times \mu^{(2)}(R)$ (blue line). For $R > 5$ all quantities in (c) have been multiplied by an additional factor 0.1. (d) *Ab initio* dipole transition moments $D_{np\sigma\,^1\Sigma_u^+ \leftarrow X\,^1\Sigma_g^+}(R)$ for $n = 3-5$ (same symbols as in (a)). (e) Energy-normalized transition moments (symbols as in (b)). (f) Dipole transition functions $d^{(0)}(R)$ and $0.1 \times d^{(1)}(R)$ (cf. Eq. (5), symbols as in (c)). The position of the ground state minimum is indicated by an arrow; the transition effectively takes place in a small range around this value.

up to the potential barrier the levels are divided into separate "inner" and "outer" vibrational progressions. For reasons discussed in Sec. III B below the frame-transformation MQDT approach is little affected by these complications up to an energy of 130 000 cm^{-1} where the inner and outer wells merge.

The quantum defect curves $\mu_{np\sigma\,^1\Sigma_u^+}(R)$ thus obtained are depicted in Fig. 1(b). The figure shows that up to ≈ 5 a.u. the $p\sigma$ quantum defect, while depending substantially on the molecular geometry, is essentially *independent* of n as one normally would expect for this type of quantity. We see therefore that the picture of a $np\sigma$ excited electron orbiting around the H_2^+ ground state core is appropriate in this range of R-values. We shall see below that our implementation of the MQDT approach enables vibrational levels reaching beyond this range to be still described quite well.

The set of clamped-nuclei quantum defect curves is further reduced to the form of an energy- and R- dependent polynomial which we define as

$$\mu(\epsilon, R) = \mu^{(0)}(R) + [\epsilon(R)]\mu^{(1)}(R) + \frac{1}{2}[\epsilon(R)]^2\mu^{(2)}(R) + \frac{m}{M}\mu^{\text{specific}}(R). \quad (2)$$

Here $\epsilon(R) = U_{np\sigma}(R) - U^+(R)$ is the binding energy of the Rydberg electron in the field of the core with the nuclei kept fixed at a distance R. The last term in Eq. (2) corresponds to the "specific" mass effect (mass polarization term) arising from the cross term $H_3' = -(m/4M)\nabla_1\nabla_2$ in the molecular Hamiltonian (where m is the electron mass and M is the nuclear reduced mass). This term couples the Rydberg and the core electrons and, as shown in Ref. 10, contributes a small mass-dependent correction to the quantum defect. H_3' has been calculated from first principles in Refs. 16 and 17. The process of reducing the three potential energy curves for $n = 3-5$ to the three functions $\mu^{(q)}(R)$, $q = 0-2$, is illustrated by Figs. 1(a)–1(c). As for each R value the number of unknowns is equal to the number of input data, Eq. (2) represents the $n = 3$, 4, and 5 *ab initio* potential energy curves *exactly*, no matter whether the Rydberg picture underlying our approach is realistic or not. On the other hand, while in the case of the $^1\Pi_u^-$ states of H_2 the same approach yielded weak energy dependences of the quantum defects (i.e., small contributions of the functions $\mu^{(1)}(R)$ and $\mu^{(2)}(R)$ to Eq. (2)), this is the case here only at short range, for R-values up to $R \approx 5$ bohrs (cf. Fig. 1(c)).

A similar procedure is applied to the *ab initio* dipole transition moments from Ref. 17 and yields energy-normalized clamped-nuclei channel transition moments. In a first step, the quantum-chemical transition moments $D_{np\sigma\,^1\Sigma_u \leftarrow X}(R)$ (Fig. 1(d)), with n chosen as explained above, are converted into energy-normalized moments $d_{np\sigma\,^1\Sigma_u \leftarrow X}(R)$ (Fig. 1(e)) through multiplication with the density-of-state factor $\partial\nu/\partial\epsilon = (n - \mu_n)^{3/2}$, where $\nu = n - \mu = (-2\epsilon)^{-1/2}$ is the effective principal quantum number and ϵ is the Rydberg binding energy in a.u. for any given R-value as above. It may again be seen that up to $R \approx 5$ a.u. these renormalized moments depend only little on the n-value so that it makes physical sense to interpret them as Rydberg channel transition moments $d_{p\sigma \leftarrow X}(R)$. Further, the ground state vibrational wavefunction is concentrated in a small range around 1.4 bohrs so that ground state absorption effectively takes place in this range. We conclude therefore that the P(1) transitions may be regarded as corresponding to the excitation of the singlet $p\sigma$ Rydberg channel. The reduced transition moments for each R are represented by an expression analogous to Eq. (2). The resulting channel dipole transition functions $d^{(0)}(R)$ and $d^{(1)}(R)$, based on the *ab initio* data for $n = 4$ and 5, for excitation from the ground state to the $p\sigma$ Rydberg channel are displayed in Fig. 1(f). In agreement with what has just been said, the function $d^{(1)}$ is found to contribute only little in the region around $R_e = 1.4$ a_0.

B. Frame transformation

Standard frame-transformation MQDT accounts for nonadiabatic coupling within the Rydberg manifold of states through vibrational-electronic quantum defect matrix elements of the form[7,10]

$$\mu^{(q,N)}_{v^+N^+,v^{+'}N^{+'}} = \int_0^{R_c} \chi_{v^+N^+}(R)\mu^{(q)}(R)\chi_{v^{+'}N^{+'}}(R)dR. \quad (3)$$

$\mu^{(q,N)}$, with index $q = 0-2$, are the quantum defect functions of Eq. (2), and $\chi_{v^+N^+}(R)$ are the vibrational eigenfunctions of H_2^+ in the vibration-rotation level v^+, N^+ of the electronic ground state of the ion with energy E_{v^+,N^+}. The superscript N ($\equiv J = 0$ in the present context) refers to the total angular momentum of the molecule H_2 exclusive of electron and nuclear spins. Since $N = 0$, we must have $N^+ = N^{+'} = 1$ in order to compensate the electron

orbital momentum $\ell = 1$. The mass-polarization term involving μ^{specific} which appears in Eq. (2) is assumed to be included with $\mu^{(0,N)}_{v^+N^+,v^{+'}N^{+'}}$ (see Ref. 7).

As detailed in Ref. 7, the integrals Eq. (3) are converted into a weakly energy-dependent reaction matrix with elements $K^{(N)}_{v^+N^+,v^{+'}N^{+'}}(E)$ ($N = 0$, $N^+ = N^{+'} = 1$) connecting various Rydberg channels v^+, N^+. Standard MQDT procedures[6,19] match the short-range electron wave functions implied by the reaction matrix $\boldsymbol{K}(E)$ for a given total energy E, to asymptotically correctly behaving phase-shifted electron Coulomb waves. It is advantageous to use a sin / cos rather than the more familiar tan formulation since in this way poles in the vibrational reaction matrix may be avoided.[19] The boundary condition then reads

$$\det|\cos\beta(E)\mathcal{S} + \sin\beta(E)\mathcal{C}| = 0, \tag{4}$$

where $\boldsymbol{K} = \mathcal{S}\mathcal{C}^{-1}$ and $\beta(E)$ is an asymptotic phase vector whose components $\beta_{v^+}(E)$ take different values depending on whether a given $N^+ = 1$ Rydberg channel is closed ($E < E_{v^+}$) or open ($E > E_{v^+}$). For closed channels $\beta_{v^+}(E) = \pi\nu_{v^+}$ with $\nu_{v^+} = (2^{-1/2})[E_{v^+} - E)]^{-1/2}$ the effective principal quantum number corresponding to that channel. For open channels $\beta_{v^+}(E) = \pi\tau_\rho$, where $\pi\tau_\rho$ denotes the set of open-channel asymptotic eigenphases to be determined by solving Eq. (4).[6] There are as many $\pi\tau_\rho$'s as there are ionization continua, i.e., thresholds E_{v^+} lower than E. Figure 3 of Ref. 9 illustrates the way different vibrational basis sets may be used in molecular MQDT calculations.

The upper limit R_c of the integral over dR in Eq. (3) was varied between $R_c \approx 15$ and ≈ 50 a.u. and the vibrational basis typically contained between 25 and 75 vibrational functions. By varying the basis size and/or the value of R_c we found that the majority of calculated levels remained unaffected to within ± 0.1 cm^{-1} or less. A few levels, particularly those corresponding to high vibrational quantum numbers, however, were found to vary up to ± 10 cm^{-1} due to interaction with the quasidiscrete levels representing the dissociation continuum of the $3p\sigma B'$ state (cf. Sec. III E below). In these cases we varied the R_c value systematically and took the average of the resonance patterns thus obtained. Specifically we proceeded by solving Eq. (4) using three different types of vibrational basis sets:

- –Restriction of the basis v^+ to closed Rydberg channels which are vibrationally bound at the energy E under consideration yields the discrete set of energies of the superexcited vibronically mixed Rydberg levels (see Sec. III C below).
- –Inclusion of all vibrationally bound channels, thus including also the ionizing open Rydberg channels, yields absorption profiles and the energy-dependent eigenphases $\pi\tau_\rho$ from which the vibrational autoionization widths Γ_{ion} are extracted (see Sec. III D below).
- –As detailed in Sec. III E below, inclusion of vibrationally bound as well as unbound channels v^+, while omitting those Rydberg channels v^+ which are open at the energy E, enables us to extract the predissociation widths Γ_{diss} of the excited Rydberg levels.

In an analogous manner, the dipole transition functions $d^{(q)}(R)$ are used to compute vibronic channel dipole transition matrix elements involving the vibrational ground state level (see Ref. 7 for details). They have the form

$$d^{(q,N)}_{v^+N^+,v''N''} = \int \chi_{v^+N^+}(R)\, d^{(q)}(R)\, \chi_{v''N''}(R) dR, \tag{5}$$

where $\chi_{v''N''}(R)$ is the vibrational wavefunction in the ground state initial level. We have $N = 0$ and $N'' = N^+ = 1$ here again as we are dealing with P(1) transitions. The quantities $d^{(q,N)}_{v^+N^+\leftarrow v''N''}$, $q = 0 - 1$, evaluated with the help of Eq. (5), are used to construct a set of energy-dependent vibronic channel transition moments $d^{(N=0)}_{v^+N^+=1\leftarrow v''=0,N''=1}(E)$ analogous to the reaction matrix $\boldsymbol{K}(E)$ (see Ref. 7 for details).

We conclude this discussion by stressing that the frame-transformation approach is an approximation in as much as it predicts non-adiabatic coupling. However, since the quantum defects determined in Sec. III A reproduce the quantum-chemical potential energy curves of the lower n-Rydberg state exactly (and assuming that the quantum-chemical energies themselves are fully converged), our calculation – if vibrationally converged – should do substantially better than the Born-Oppenheimer or adiabatic approximation. Indeed, when the vibrational motion is frozen altogether, the MQDT boundary condition Eq. (4) reverts to the Rydberg expression Eq. (1) which we used at the outset to obtain the quantum defect functions.

C. Bound levels and discrete line intensities

Bound levels are calculated by using the first type of vibrational basis set discussed in Sec. III B. Once an energy $E = E_n$ has been found such that Eq. (4) is satisfied, the level energy taken relative to the ionization potential and in wavenumber units becomes

$$[(E_n - E^+_{v^+=0,N^+=0})/hc] = -\frac{\mathcal{R}_{H_2}}{[\nu_{v^+=0,N^+=0}(E_n)]^2}, \tag{6}$$

where $\mathcal{R}_{H_2}$ is the mass-corrected Rydberg constant and E_n is the level energy in joules. Note that the use of the mass corrected Rydberg constant instead of $\mathcal{R}_\infty$ is equivalent to including the term $-(m/2M)\nabla^2_1$ of the molecular Hamiltonian, which in the standard approach is a part of the adiabatic correction.[10] The effective transition moment to a bound Rydberg level n is given by the following superposition of channel amplitudes:

$$D_n = \frac{1}{\mathcal{N}} \sum_k d_{k,k''}(E_n) B_k(E_n), \tag{7}$$

where B_k are the channel mixing coefficients obtained by solving Eq. (4) and where k stands for the ionization channels v^+, $N^+ = 1$, and k'' stands for $v'' = 0$, $N'' = 1$. $\mathcal{N}$ is the overall normalization factor of the bound state wavefunction, see, e.g., Ref. 7 for detailed discussion and expressions. The transition moment D_n for each particular spectral line is finally converted into an upper state emission probability by

means of the relation

$$A_{n\to v''N''} = \frac{4}{(2N+1)}\frac{mc^2}{\hbar}\alpha^5\left(\frac{E_n - E_{v''N''}}{2\mathcal{R}hc}\right)^3\left|\frac{D_n}{a_0}\right|^2$$
$$= 6.426\times 10^{10}\left(\frac{1}{2N'+1}\right)$$
$$\times\left(\frac{E_n - E_{v''N''}}{2\mathcal{R}hc}\right)^3\left|\frac{D_n}{a_0}\right|^2\ \mathrm{s}^{-1}. \quad (8)$$

Here α is the fine structure constant. The transition energy $E_n - E_{v''N''}$ is in joules and the transition moment D_n is in meters. The ratios in the brackets $(\ldots)$ and $|\ldots|$ correspond, respectively, to the transition energy and to the dipole transition moment in atomic units.

D. Ionization continuum

Using the second type of vibrational basis set discussed in Sec. III B we may also take account of the ionization channels which are open. This is done by replacing $\pi\nu$ in Eq. (4) by $-\pi\tau_\rho$ for every channel which is open. The normalization of the continuum wavefunction is also different from that applied to the bound levels, as described in detail in Ref. 9.

The total photoionization intensity which is of interest here is expressed in terms of a set of real dipole amplitudes which replace Eq. (7),

$$D_\rho(E) = \sum_{k=1} d_{k,k''}(E)B_k^{(\rho)}(E). \quad (9)$$

The total ionization cross section is then proportional to

$$[D(E)]^2 = \sum_{\rho=1}^{N_P}[D_\rho(E)]^2, \quad (10)$$

where N_P is the number of channels which are open at the energy E. The total photoionization cross section becomes

$$\sigma(E) = \frac{4}{(2N''+1)}\pi^2\alpha(E - E_{v''N''})\,[D(E)]^2, \quad (11)$$

where again α denotes the fine structure constant. Here D^2 has dimension $[E^{-1}L^2]$ so that $(E - E_{v''N''})D^2$ has dimension $[L^2]$. Therefore, if, for instance, the dipole operator implicit in Eq. (5) has been written in bohr units, the cross section will be in a_0^2.

E. Dissociation continuum

The competition between ionization and dissociation channels constitutes a problem of molecular Rydberg dynamics in general. The inclusion of dissociation channels into the MQDT framework has been described in previous papers.[19,22,23] Here we are concerned with reasonably narrow and isolated line profiles so that the approach described in those papers may be greatly simplified since we are able to neglect the interference between ionization and dissociation processes. We proceed as follows. Our treatment of dissociation is based upon the realization that the dissociating state in the present problem is primarily the $3p\sigma B'$ state and as such is simultaneously a member of the $p\sigma$ ionization channel (which we are considering here), and therefore plays a double role. This implies that the non-adiabatic coupling leading to vibrational autoionization of the $np\sigma$ manifold above threshold *is the same* as that causing predissociation by the $3p\sigma B'$ state. Therefore, the vibronic quantum defect matrix elements $\mu^{(q,N=0)}_{v^+N^+,v^{+\prime}N^{+\prime}}(E)$ of Eq. (3) contain *all* the information required to evaluate the predissociation widths in addition to the autoionization widths. A detailed description of this simplified treatment of dissociation has been given in Ref. 9.

IV. RESULTS

The absorption spectrum has been recorded in the range of 81.2–75.0 nm. Thirty one new P(1) transitions have been assigned or reassigned and are collected in Table I along with 36 P(1) lines which have been observed previously in this range[5,11,12] and which have been remeasured here.

A. Line positions and assignments

As in our previous papers, we compared in a first step our calculated line positions with experimental absorption data published previously.[5,24,25] A few P(1) transitions have also been observed in three-photon 2+1 double resonance ionization spectroscopy (see Ref. 26, and references therein). Figure 2(a) displays the differences $E(\mathrm{obs}) - E(\mathrm{calc})$ for 65 P(1) transitions reported in the literature. As can be seen from the histogram representing the same data points (Fig. 2(c)) the agreement is within 1 cm^{-1} for the vast majority of previously observed P(1) transitions. This fact confirms the reliability of the MQDT calculations, which therefore may be used to assign new P(1) transitions. We note that the agreement displayed in Figs. 2(a) and 2(c) is somewhat less good than we obtained previously for the Q(N) transitions,[7] but we also note that the non-adiabatic interactions here are far stronger than in the previously studied case. In particular, the P(1) transitions corresponding to $n = 3$ upper levels ($B'^1\Sigma_u^+$ ($B3$) state) are reproduced only to within about 2 cm^{-1} (cf. the lowest-energy points in Fig. 2(a)). This is no doubt due to the fact that the B' state interacts significantly with high levels of the $n = 2$ B state ($B2$) which in turn, for reasons discussed in Sec. III A, are only moderately well described within the framework of the simple MQDT approach employed here.

In a next step, we compared our measured line frequencies with previous measurements where these are available, in order to assess the uncertainty of our experimental energies. It turns out, as in our previous study,[9] that the agreement is to within 1 cm^{-1} or better.

For wavelengths shorter than 80 nm many H_2 absorption lines still remain unassigned today despite the comprehensive work of Ref. 5. Wolniewicz *et al.*[27] published a fully *ab initio* non-adiabatic calculation of excited $^1\Sigma_u^+$ levels up to $n = 6$, the accuracy of which is estimated to be about 1 cm^{-1}. However, this work was restricted to levels which are not predissociated significantly and correspond to rather low n values. We have found that in several cases our measurements agree better with the theoretical values than the previously published measurements. In addition, the present MQDT calculations allow us to propose a number of new assignments:

TABLE I. P(1) transitions in ground state absorption of H_2.

State	v	λ(obs)	E(obs)	E(obs)-E(calc)	A(obs)	A(calc)	Γ(obs)	Γ(calc)
$6p\sigma$	1	81.13667	123 248.8	0.0	58 ± 6	45.2	0.3 ± 0.6	0.00
$11p\sigma$	0	81.02554	123 417.9	−0.3	10 ± 3	9.0		
$12p\sigma$	0	80.92618	123 569.4	− 0.2		5.0		
$13p\sigma$	0	80.84914	123 687.2	− 0.3	2.8 ± 1.2	2.5		
$5p\sigma$	2	*80.80577*	*123 753.5*	*0.3*	155 ± 18	127.4	0.0 ± 0.6	0.00
$14p\sigma$	0	80.78771	123 781.2	0.1	7.7 ± 1.3	6.5		
$15p\sigma$	0	80.73887	123 856.1	0.0	3.3 ± 1.1	2.6		
$17p\sigma$	0	80.66617	123 967.7	− 0.7	3.3 ± 1.9	1.2		
$26p\sigma$	0	**80.52876**	**124 179.2**	**0.0**	4.9 ± 1.5	2.7		
$4p\sigma$	4	80.52238	124 189.1	0.3	344 ± 37	166.6	1.3 ± 0.3	1.67
$7p\sigma$	1	*80.51931*	*124 193.8*	*0.0*	133 ± 18	63.1	0.2 ± 0.3	0.00
$27p\sigma$	0	**80.51202**	**124 205.1**	**0.1**	13 ± 1	8.0		
$28p\sigma$	0	**80.50499**	**124 215.9**	**0.2**	4.1 ± 0.9	3.4		
$8p\sigma$	1	80.17442	124 728.1	0.7	29 ± 3	32.6	4.29 ± 0.64	4.79
$9p\sigma$	1	79.93016	125 109.2	0.5	8.0 ± 2.3	8.8	3.01 ± 1.39	3.28
$6p\sigma$	2	**79.84624**	**125 240.7**	**−0.1**	26 ± 8	31.9	0.08 ± 0.66	0.28
$10p\sigma$	1	79.74416	125 401.0	0.3	18 ± 4	19.7	2.55 ± 0.66	2.72
$5p\sigma$	3	*79.62851*	*125 583.2*	*− 0.8*	2.8 ± 0.4	2.7	0.33 ± 0.65	0.23
$11p\sigma$	1	79.61538	125 603.9	− 0.8	20 ± 7	15.4	0.60 ± 0.69	1.81
$4p\sigma$	5	79.53543	125 730.1	− 0.7	491 ± 51	271.5	0.91 ± 0.31	1.53
$12p\sigma$	1	**79.52013**	**125 754.3**	**−0.2**	44 ± 5	40.5	0.98 ± 0.65	1.66
$13p\sigma$	1	**79.44541**	**125 872.6**	**0.4**	5.3 ± 2.2	8.6	0.48 ± 0.94	1.53
$14p\sigma$	1	79.3866	125 965.8	0.0	3.4 ± 0.5	4.8	0.53 ± 0.66	1.22
$18p\sigma$	1	79.24602	126 189.3	− 0.7	22 ± 7	15.7	0.37 ± 0.64	0.11
$7p\sigma$	2	79.23302	126 210.0	− 0.3	79 ± 9	50.3	0.33 ± 0.64	0.38
$19p\sigma$	1	79.21615	126 236.9	− 0.1	20 ± 2	17.4	0.37 ± 0.27	0.60
$20p\sigma$	1	79.19798	126 265.8	− 0.2	8.6 ± 1.1	8.1	0.38 ± 0.35	0.54
$21p\sigma$	1	79.18167	126 291.9	0.0	3.3 ± 2.0	5.2		0.49
$22p\sigma$	1	79.16733	126 314.7	0.4	1.9 ± 2.0	3.7	0.96 ± 0.71	0.46
$23p\sigma$	1	79.15541	126 333.8	− 0.3	2.3 ± 1.0	2.9	0.77 ± 0.73	0.44
$24p\sigma$	1	79.14405	126 351.9	0.5		2.3		0.29
$8p\sigma$	2	78.8834	126 769.4	0.6	31 ± 4	30.9	13.66 ± 0.92	13.81
$4p\sigma$	6	78.75521	126 975.7	− 0.7	91 ± 9	54.0	1.51 ± 0.35	2.07
$9p\sigma$	2	78.62457	127 186.7	1.4	14 ± 2	13.8	7.04 ± 1.48	7.10
$10p\sigma$	2	78.47366	127 431.3	− 0.8	43 ± 8	39.1	1.96 ± 0.66	2.44
$5p\sigma$	4	*78.44488*	*127 478.0*	*−0.6*	182 ± 19	186.2	3.71 ± 0.66	4.30
$11p\sigma$	2	78.33504	127 656.8	0.5	25 ± 3	23.3	5.70 ± 0.79	5.72
$12p\sigma$	2	78.24136	127 809.6	0.6	11.5 ± 1.3	11.1	3.74 ± 0.77	4.55
$15p\sigma$	2	**78.07163**	**128 087.5**	**−0.8**	8.4 ± 0.9	5.9	0.21 ± 0.66	0.43
$7p\sigma$	3	78.05005	128 122.9	− 0.6		35.8	1.30 ± 0.68	0.80
$16p\sigma$	2	78.02296	128 167.4	− 1.0	12 ± 2	10.2	1.77 ± 1.09	1.90
$4p\sigma$	7	78.01054	128 187.8	0.0	132 ± 14	81.2	2.02 ± 0.33	2.11
$18p\sigma$	2	77.96748	128 258.6	− 0.3	9.4 ± 3.2	7.6	0.72 ± 1.04	1.39
$20p\sigma$	2	77.92704	128 325.2	0.0	4.7 ± 1.7	4.1		1.05
$22p\sigma$	2	77.89742	128 374.0	− 0.4	1.4 ± 0.6	2.6	0.0 ± 0.9	0.74
$8p\sigma$	3	*77.71776*	*128 670.7*	*0.4*	31 ± 4	25.4	7.63 ± 0.79	12.53
$5p\sigma$	5	*77.41919*	*129 166.9*	*0.6*	89 ± 9	97.8	6.02 ± 0.70	7.12
$4p\sigma$	8	77.35089	129 281.0	0.6	154 ± 16	99.8	1.82 ± 0.34	
$10p\sigma$	3	**77.28889**	**129 384.7**	**−0.6**	25 ± 8	29.0	4.70 ± 2.10	10.70
$11p\sigma$	3	**77.16822**	**129 587.0**	**2.1**	16 ± 2	13.9	7.32 ± 0.77	7.78
$12p\sigma$	3	**77.07856**	**129 737.8**	**0.4**	7.6 ± 2.3	4.4	1.30 ± 0.70	6.75
$13p\sigma$	3	**77.01386**	**129 846.8**	**−1.3**	1.0 ± 1.0	1.1	3.29 ± 1.17	2.27
$7p\sigma$	4	*76.97919*	*129 905.2*	*−1.2*	72 ± 9	36.4	1.86 ± 0.72	1.06
$14p\sigma$	3	**76.94154**	**129 968.8**	**−0.6**	23 ± 3	23.1	4.95 ± 2.09	4.76
$17p\sigma$	3	76.83285	130 152.7	0.7	6.7 ± 1.3	5.6	2.83 ± 0.77	2.60
$4p\sigma$	9	*76.80508*	*130 199.7*	*−1.5*	12 ± 2	4.3	1.65 ± 0.34	
$5p\sigma$	6	*76.74199*	*130 306.8*	*−0.7*	40 ± 5	23.5	0.85 ± 0.71	0.20
$6p\sigma$	5	*76.47987*	*130 753.4*	*−0.2*	118 ± 14	80.7	0.87 ± 0.69	0.72
$9p\sigma$	4	*76.37907*	*130 925.9*	*0.1*	67 ± 7	51.3	12.92 ± 0.86	15.49

TABLE I. (*Continued.*)

State	v	λ(obs)	E(obs)	E(obs)-E(calc)	A(obs)	A(calc)	Γ(obs)	Γ(calc)
$4p\sigma$	10	*76.29521*	*131 069.8*	*−0.7*	22 ± 2	26.5	1.70 ± 0.36	
$7p\sigma$	5	**75.99347**	**131 590.3**	**−0.1**	28 ± 3	33.8	4.48 ± 0.88	5.42
$5p\sigma$	7	*75.95632*	*131 654.6*	*−6.6*	20 ± 3	20.9	0.0 ± 0.7	0.07
$6p\sigma$	6	**75.57402**	**132 320.6**	**−2.9**	60 ± 7	51.2	9.90 ± 1.20	12.20
$5p\sigma$	8	*75.24647*	*132 896.6*	*−3.6*	41 ± 4	40.2	5.16 ± 0.73	5.51
$7p\sigma$	6	**75.11049**	**133 137.2**	**4.1**		0.7	7.36 ± 0.97	9.30
$6p\sigma$	7	**74.88104**	**133 545.2**	**−1.4**	10 ± 2	13.4	1.66 ± 0.82	0.74
$7p\sigma$	7	**74.34290**	**134 511.8**	**2.2**		11.9	12.48 ± 2.34	11.33

λ, observed wavelength (nm).
v, upper state vibrational quantum number (main component in the wavefunction expansion resulting from Eq. (4)).
$E = \nu/c$, transition energy (cm^{-1}). Upper state energy levels are obtained by adding the energy of the $X^1\Sigma_g^+$, $v'' = 0$, $N'' = 1$ level, *viz.* 118.49 cm^{-1}.
$E_{obs} - E_{calc}$, difference of observed and calculated level energies (cm^{-1}).
A, emission probability toward $X^1\Sigma_g^+$, $v'' = 0$, $N'' = 1$ (10^5 s^{-1}).
Γ, width (FWHM) (cm^{-1}). The calculated values correspond to ionization partial widths, Γ_{ion}, except vor the $4p\sigma$, v levels where the dissociation partial width Γ_{diss} is given.
Reassigned lines are indicated in italics. Transitions reported here for the first time are indicated in boldface. The remaining assignments are from Refs. 5, 12, and 26 except for $4p\sigma$, $v = 4$ and 5 which were corrected in Ref. 10.

–$4p\sigma\, B''\bar{B}\,^1\Sigma_u^+$ state ($B4$): This state has been the subject of an earlier study[12] where the rotational line intensities of $B''\bar{B}\,^1\Sigma_u^+, v, N = 0 \leftarrow X^1\Sigma_g^+, v'' = 0, N'' = 1$ transitions were reported and compared with theoretical calculations made in the adiabatic approximation. These transitions have strong absorption intensity to the extent that the vibrational wavefunctions of the corresponding upper levels are located in the inner-well of the $B''\bar{B}$ state. These levels are strongly predissociated by the B' state and were not considered in the non-adiabatic calculations of Ref. 27. The present MQDT calculations give far better agreement between experiment and calculation than the adiabatic approximation employed in Ref. 12, $\approx \pm 1$ cm^{-1} as compared to $\approx \pm 50$ cm^{-1}. The assignments of these levels are corroborated by the MQDT calculations, and their energies are now determined more precisely than before. The new energy levels and transition probabilities have lead us to re-assign the P(1) transitions associated with the inner well levels $v = 9$ and 10 of the $B''\bar{B}$ state.

Levels lying higher than the $B''\bar{B}$ potential barrier have probability amplitude both in the inner and in the outer well and therefore have a small but measurable transition probability in absorption from the ground state. These levels are only weakly predissociated and were calculated in the work of Ref. 27. We believe that these values are more accurate than those obtained by MQDT which does not provide an equally accurate description of the outer well of the $B''\bar{B}$ state as the coupled-equations approach.

–$5p\sigma\,^1\Sigma_u^+$ state ($B6$): The situation for this state is similar to that for $B''\bar{B}$ in that only the $v = 0$ and 1 upper levels have been calculated in Ref. 27 and no intensities were given there. On the other hand, the adiabatic calculations of Ref. 12 are of insufficient quality for a meaningful comparison with experiment. We are now in a position to re-examine the earlier assignments. We have found that most of these are not valid and we have reassigned the levels $v = 3$ to 8.

–$6p\sigma\,^1\Sigma_u^+$ state: The levels $v = 2$, 5, 6, and 7 are observed here for the first time. The transitions from $v'' = 0$ to $v = 3$ and 4 are calculated to have very low intensity, in agreement with the observations where no corresponding absorption lines can be detected in the spectrum.

–$7p\sigma\,^1\Sigma_u^+$ state: The levels $v = 5$, 6, and 7 are reported here for the first time.

–Higher $np\sigma$ states: Using our MQDT calculations we have been able to extend the assignments made in Ref. 5. However, as previously in Ref. 5, it was found that the P(1) series converging toward the $v^+ = 4$, $N^+ = 1$ ionization limit is too much broadened and/or too faint to be detected. The energy given in Ref. 5 for the transition to $8p\sigma$, $v = 3$, $N = 0$ must be a misprint and should be 128 670.2 instead of 128 679.2 cm^{-1}. This line corresponds to the isolated point in Fig. 2(a).

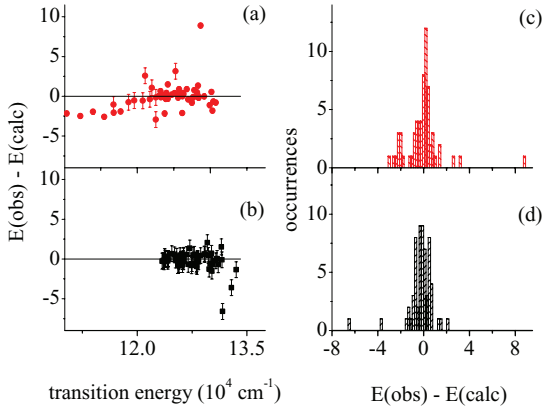

FIG. 2. Differences $E(obs) - E(calc)$ in cm^{-1} between observed $N = 0$ *ungerade* singlet level positions in H_2 $^1\Sigma_u^+$ and those obtained in the present MQDT calculations, plotted versus the transition energy. (a) Previous measurements (see Refs. 5 and 24–26) and (b) present experiment. (c) Histogram showing the overall agreement obtained in (a). A Gaussian fit of the distribution yields a mean deviation -1.45 cm^{-1} and a width 0.187 cm^{-1}. (d) histogram showing the overall agreement obtained in (b). A Gaussian fit of the distribution yields a mean value -0.96 cm^{-1} and a width 0.315 cm^{-1}.

–Local perturbations, blended lines, and complex resonance: The absorption spectrum exhibits two strong blended lines near 123 750 cm^{-1}. According to the calculations the higher of these corresponds to the P(1) transition to $5p\sigma$, $v = 2$, $N = 0$. Reference 5 reports the transition energies 123 754.1 and 123 751.0 cm^{-1} for the pair, respectively, and it was the lower-frequency line that was assigned to this transition, whereas the upper one was left unassigned. In view of our present calculations we propose to change the assignment. The P(1) lines leading to $7p\sigma$, $v = 1$, $N = 0$ and $4p\sigma$, $v = 4$, $N = 0$ are partially blended. A two-peak fit of the linear intensity plot has allowed us to obtain an improved value for the former: 124 193.8 instead of 124 195.3 cm^{-1} as given in Ref. 5. The assignments of the two lines are inverted here in agreement with Ref. 10 where $4p\sigma$, $v = 4$, $N = 0$ had already been corrected. A similar procedure was applied to the blended pair of lines consisting of the P(1) transition to $6p\sigma$, $v = 2$, $N = 0$ and the broad R(0) transition to $9p\sigma$, $v = 1$, $N = 1$. Finally, we mention a complex absorption feature which appears near the predicted position of $6p\sigma$, $v = 6$, $N = 0$ and which has an apparent width of about 10 cm^{-1}: our calculations show that this level is strongly mixed with the manifold of high-n levels ($n \approx 45$) converging toward the $v^+ = 3$, $N^+ = 1$ threshold. Figure 3 shows that this "complex" resonance,[28] although completely blurred by blending, is clearly visible in the experimental spectrum. The width given in Table I corresponds to the overall width of the complex resonance.

Figure 2(b) displays the residuals $E(\text{obs}) - E(\text{calc})$ for the 67 P(1) lines measured here. Figure 2(d) is the corresponding histogram. The agreement is better than 1 cm^{-1} except for the three lines corresponding to $5p\sigma$, $v = 7$, $N = 0$, $5p\sigma$, $v = 8$, $N = 0$ and $6p\sigma$, $v = 7$, $N = 0$ which are located above the barrier of the $4p\sigma B''\bar{B}$ state. Fourteen of the new P(1) lines reported in Table I had been observed previously and have been corrected here. Seventeen more P(1) transitions are assigned here for the first time (cf. Table I).

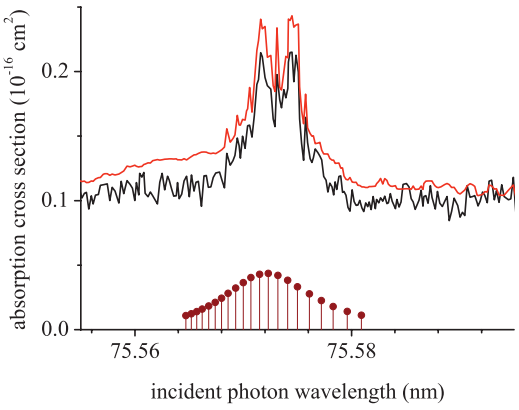

FIG. 3. Experimental spectra in the region of the $6p\sigma$, $v = 6$, $N = 0$ level. (Upper trace) Black: observed absorption cross section. Red: observed ionization excitation cross section. (Lower trace) calculated discrete absorption lines plotted on an arbitrary scale.

B. Line intensities

We have extracted Einstein coefficients corresponding to each observed line using the relation

$$\int \sigma d\lambda = \frac{\lambda^4}{8\pi c} A_{v',v''}\, n_{N''}\, h(N', N'') = \frac{\lambda^4}{8\pi c} A_{v',v''} \frac{0.65}{3}. \quad (12)$$

Here σ is the measured absorption cross section which is integrated over the profile of a given line, and λ is the wavelength. $n_{N''}$ is the fraction of molecules in the rotational state $N'' = 1$ (≈ 0.65 for ordinary hydrogen at room temperature). $h(N', N'') = (2N' + 1)/(2N'' + 1)$ is the ratio of the statistical weights of the upper and lower levels ($= 1/3$ for a P(1) transition). The area of each peak was evaluated by means of a Gaussian fit.

Apart from the problem of correctly assigning the transitions, the main difficulty encountered in the intensity determinations arose when different absorption lines are blended. In such circumstances the simultaneous use of the absorption spectra together with the ionization and dissociation excitation spectra turned out to be helpful. This is because, for instance, a single composite structure may be visible in absorption, whereas distinct features appear in the ionization and dissociation excitation spectra at slightly different positions. Examining the dynamical behavior of a given upper level thus allows the assignment of the upper level to be ascertained and its Einstein coefficient to be determined. The error bars given in Table I take account of the statistical errors and the calibration uncertainties.

Figure 4 compares the measured and calculated Einstein A values for the $np\sigma$, $n = 4-9$ levels in the 81−74 nm region. Figure 5 displays analogous information for the higher-n Rydberg members converging to the $v^+ = 0-3$, $N^+ = 1$ vibrational ion thresholds. Data points representing calculations made in the adiabatic approximation are also included in these two figures (black lines). The adiabatic approximation is seen to predict a smooth variation of the line intensities with v and n, corresponding to the Franck-Condon envelope (Fig. 4) and the $1/n^3$ Rydberg scaling factor (Fig. 5). By contrast, the MQDT calculations (blue lines), which take account of non-adiabatic (vibronic) coupling, predict a far less smooth behavior for the same quantities. The observed data points follow these predicted irregular variations rather closely.

In Fig. 6 the ratios $A(\text{obs})/A(\text{calc})$ of the experimental and the theoretical Einstein coefficients are plotted for all measured lines versus the transition energy, both using the theoretical values calculated in the adiabatic approximation and those obtained with the MQDT approach. It may be seen that the former yield ratios that deviate strongly from unity, with $A(\text{obs})/A(\text{calc})$ ranging from ≈ 0.018 to ≈ 27. This behavior underlines the importance of the non-adiabatic perturbations which are neglected in the adiabatic approximation. The ratios based on MQDT calculations are much closer to unity in the average, and range from 0.5 ± 0.5 ($22p\sigma$, $v = 1$, $N = 0$ at 126 314.7 cm^{-1}) to 2.8 ± 1.6 ($17p\sigma$, $v = 0$, $N = 0$ at 123 967.7 cm^{-1}). These extrema correspond to upper levels which inherently absorb very weakly, but the intensities of which are substantially enhanced by non-adiabatic interaction. A slight inaccuracy of the calculated perturbation

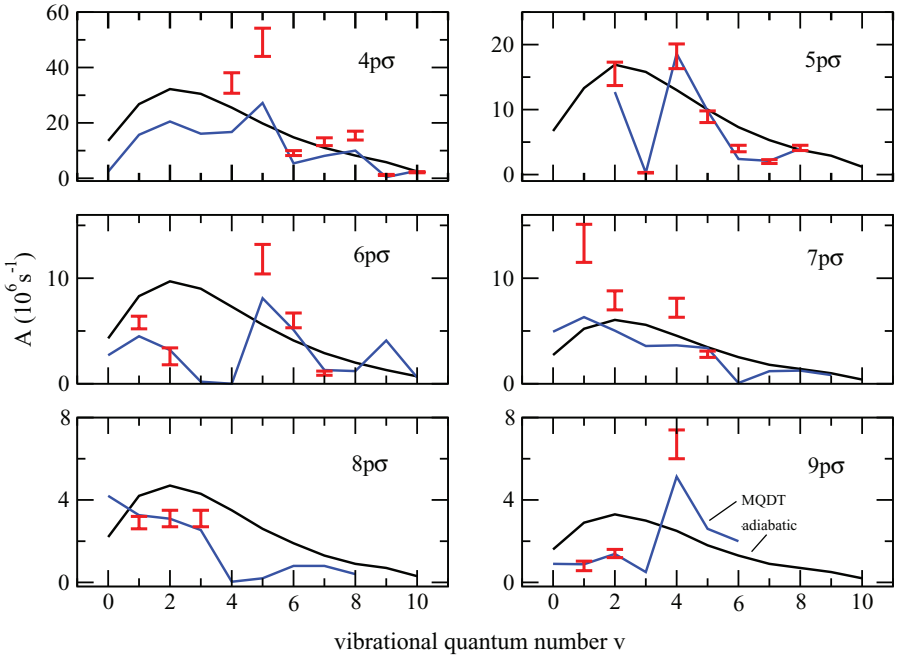

FIG. 4. Einstein A coefficients for P(1) transitions in H_2 ($np\sigma\ ^1\Sigma_u^+$, v, $N = 0 \leftarrow X^1\Sigma_g^+$, $v'' = 0$, $N'' = 1$ for $n = 4$–9 plotted versus the upper state vibrational quantum number v. Red error bars: measured values. Black lines: theory, adiabatic approximation. Blue lines: theory, non-adiabatic (MQDT). The vibrational quantum numbers given for $4p\sigma$ correspond to the inner well of the $B''\bar{B}$ state.

therefore strongly affects the resulting theoretical line intensity. At the same time the measurement of these weak lines is affected by a large relative error (cf. Fig. 6). The agreement between experimental and theoretical intensities is not as good as we found previously[9] for the Q(N) transitions of H_2, but it must be remembered that the perturbations are much stronger here.

C. Competition between decay pathways and line widths

We have not found a single P(1) transition that appears in the fluorescence channel and whose upper level lies higher than the ionization energy. Only a handful of such transitions yield a signal in the dissociation excitation spectrum. Among these the lines originating from the $4p\sigma B''$ inner well of the $B''\bar{B}$ state are observed predominantly in the dissociation channel. Some levels belonging to the $5p\sigma$ state share their decay between the ionization and the dissociation channels. All of the remaining transitions yield a measurable signal only in the ionization channel.

Experimental total widths have been obtained by deconvolution of the observed line profiles with the apparatus function. Figures 7 and 8 show two examples of observed resonances from which the total width has been extracted (Table I). Figure 7 displays a broad resonance which is fully ionized through vibrational autoionization. Figure 8 illustrates a case where the width is much smaller and predissociation

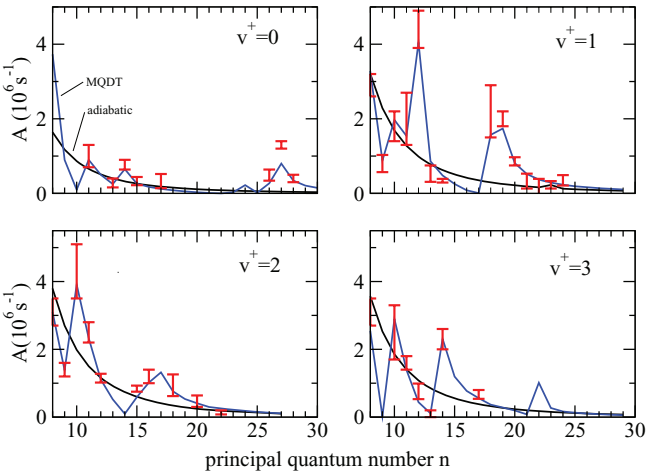

FIG. 5. Einstein A coefficients for P(1) transitions in H_2 ($np\sigma\ ^1\Sigma_u^+$, v^+, $N = 0 - X^1\Sigma_g^+$, $v'' = 0$, $N'' = 1$), for $v^+ = 0$–3, $n > 7$. Symbols as in Fig. 4.

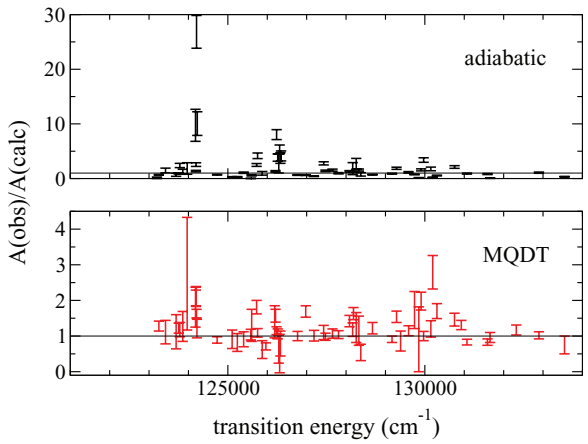

FIG. 6. Ratios of experimental and theoretical Einstein A coefficients for P(1) absorption transitions in H_2, plotted versus the transition energy. (Upper panel) Adiabatic approximation. (Lower panel) MQDT.

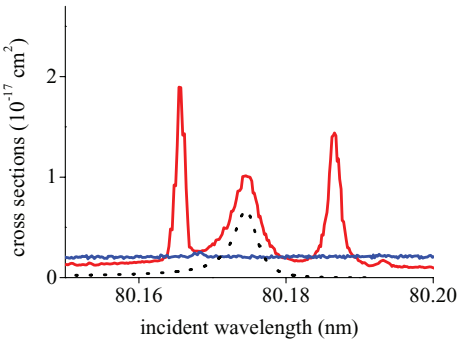

FIG. 7. Autoionizing resonance: Observed photoionization (red trace) and photodissociation (blue trace) cross sections of H_2 near the $8p\sigma$, $v = 1$, $N = 0$ resonance ($v'' = 0$, $N'' = 1$). Theoretical (MQDT) P(1) photoionization cross section (dashed black trace).

dominates. Recall that the vibronic coupling that causes the decay is the same in both examples. In general, the process is favored which requires the smaller amount of interconversion of vibrational and electronic energy. In line with this "vibrational propensity rule"[29,30] the superexcited level with the lower v value preferentially autoionizes ($v = 1$, the vibrational energy is decreased in the process, Fig. 7), whereas the upper state with the higher v value preferentially predissociates ($v = 5$, the vibrational energy is increased in the process, Fig. 8).

Figure 9 is a plot of the theoretical photoionization spectrum, evaluated by means of Eq. (11) by neglecting the alternative decay paths dissociation and fluorescence. In the lower panel, a logarithmic scale has been used in order to accommodate the widely varying intensities of the resonances. Some of the resonances are seen to exceed the continuum background by two or three orders of magnitude. These resonances are the only ones that appear when a linear scale is used (upper panel of Fig. 9). They have high peak intensities because their autoionization decay widths are quite small, small enough so that the slow dissociation process can enter into competition. Indeed, it turns out that the upper levels of these resonances belong to the $4p\sigma B''$ inner well vibrational progression of the $B''\bar{B}$ state which are predominantly predissociated (cf.

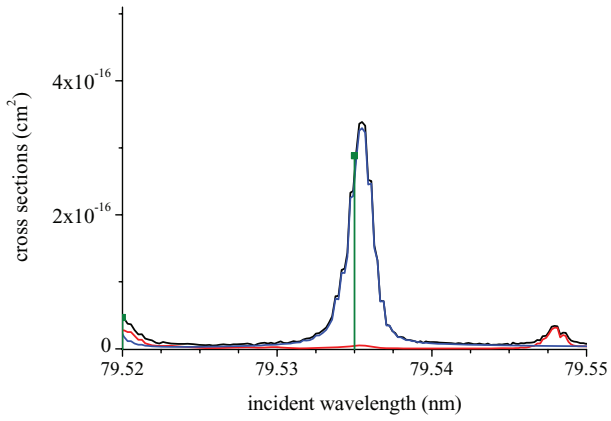

FIG. 8. Predissociating resonance: Observed photoionization (red trace) and photodissociation (blue trace) cross sections of H_2 near the $4p\sigma$, $v = 5$, $N = 0$ resonance ($v'' = 0$, $N'' = 1$). Theoretical (MQDT) P(1) discrete line intensity (green vertical bar).

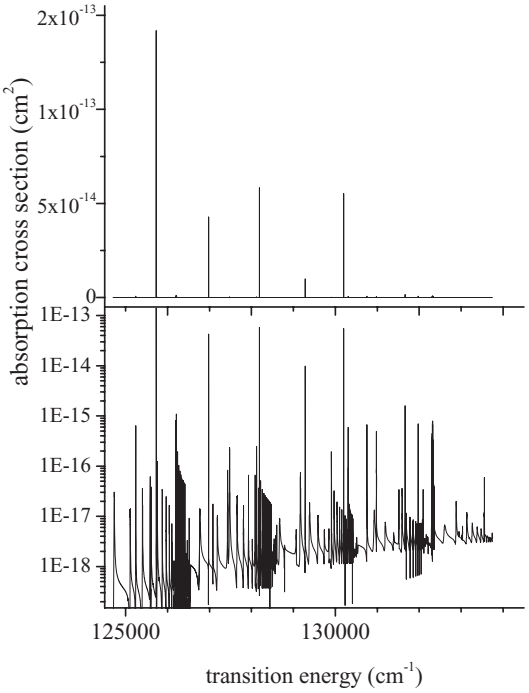

FIG. 9. Theoretical P(1) photoionization cross section, calculated with MQDT, plotted versus the transition energy. (Upper trace) linear intensity scale. (Lower trace) logarithmic intensity scale.

Fig. 8). In the case of the yet much narrower Q(N) resonances studied in Ref. 9 it was the fluorescence decay process that entered into successful competition with autoionization.

We have extracted the theoretical ionization partial line widths Γ_{ion} from Lorentzian fits of the resonances of the calculated photoionization cross section. Figure 10 compares the calculated autoionization widths with the total widths Γ_{tot} derived from experiment. The overall agreement of the irregularly varying observed widths and the calculated autoionization widths is conspicuously good, showing that vibrational autoionization is indeed the main cause for the broadening of the P(1) lines. Predissociation, even when it dominates, is comparatively slow. It affects only experimental data points situated near the abscissa in the figure, and its contribution is hardly visible on the linear scale of Fig. 10.

Figures 11 and 12 are analogous to the previous Figs. 4 and 5 for the line intensities and provide a more detailed view

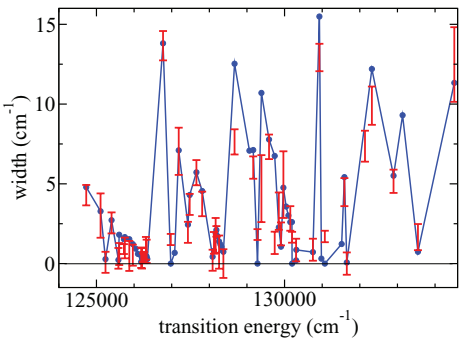

FIG. 10. Line widths (FWHM) of P(1) absorption transitions in H_2, plotted versus the transition energy. Red error bars: measured values Γ_{tot}. Blue dots connected by lines: calculated ionization partial widths Γ_{ion} (MQDT).

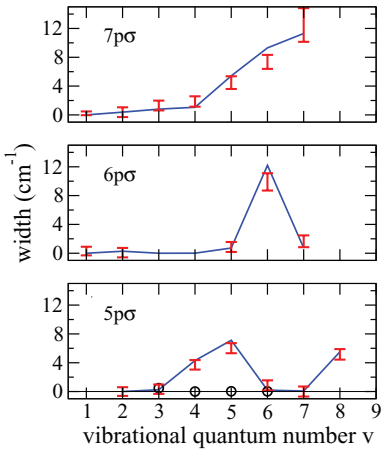

FIG. 11. Line widths (FWHM) of P(1) absorption transitions in H_2, plotted for $n = 5-7$ versus the upper state vibrational quantum number v. Red error bars: measured widths. Blue lines: calculated ionization partial widths Γ_{ion} (MQDT). Black circles: calculated dissociation partial widths Γ_{diss} (MQDT).

of the observed and calculated decay widths. The crucial role played by the vibronic interactions is again illustrated. In particular, the calculations indicate that the lower-n P(1) transitions (Fig. 11) are more or less perturbed depending on the proximity of an interacting $4p\sigma B''$ state level. The resulting widths may thus change by orders of magnitude, allowing dissociation to occur in some cases. Figure 12 provides another striking illustration of the vibrational "propensity rule" which here favors a $\Delta v = 1$ as compared to a $\Delta v = 2$ autoionization process: for $v = 2$ and 3 (upper two panels of Fig. 12), the levels with principal quantum numbers $n < 8$ can autoionize only by interconversion of at least two vibrational quanta since they lie just below the $v^+ - 1$ ionization threshold (arrows in the figure). The $n = 8, v$ level which lies just above the $v^+ = v - 1$ threshold, however, may decay into that ionization continuum by interconversion of a *single* vibrational quantum. The order of magnitude increase of the autoionization widths at this point is clearly seen in Fig. 12. For $n > 8$ the autoionization widths decrease basically according to the

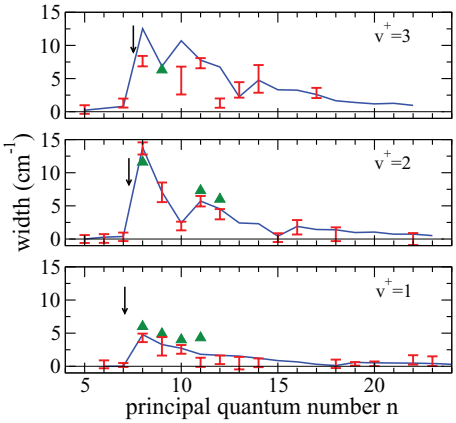

FIG. 12. Line widths of P(1) absorption Rydberg series in H_2, plotted for $v^+ = 1-3$ versus the upper state principal quantum number n. Red error bars: measured values (this work). Green triangles: previously measured values (Dehmer and Chupka[11]). Blue lines: calculated ionization widths Γ_{ion} (MQDT). The arrows indicate the positions of the vibrational ionization thresholds $v^+ - 1$.

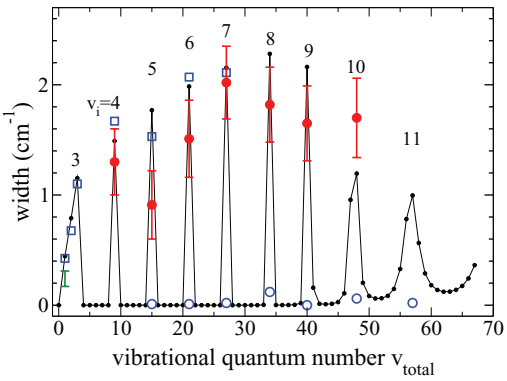

FIG. 13. Widths of the $4p\sigma B''\bar{B}\ ^1\Sigma_u^+$ $(B4)$ $N = 0$ levels plotted versus the double-well vibrational quantum number v_{total}. The vibrational quantum number corresponding to the inner well, v_i, is indicated at the top. Red dots with error bars: measured values (present work). Green error bar: measured value from Dehmer and Chupka (Ref. 11). Open blue squares: theoretical dissociation widths (MQDT), calculated for levels confined to the inner potential well of the $B''\bar{B}$ state. Open blue circles: calculated ionization widths (MQDT) for inner well states. Black dots connected by lines: perturbative vibronic coupling calculation of predissociation widths.

n^{*-3} Rydberg scaling rule, but are in addition perturbed by local interactions.

Figure 13 displays the experimental and theoretical decay widths of the $4p\sigma B''\bar{B}$, $N = 0$ levels. The autoionization partial widths Γ_{ion} calculated by MQDT for the inner well vibrational states (blue open circles) are quite small, corresponding to lifetimes of the order of nanoseconds. This means that fluorescence could occur if the dissociation process was not much faster. The plot shows that the dissociation widths calculated for the inner-well levels (blue open squares), also calculated by MQDT, are of the order of several cm^{-1}, implying that dissociation occurs on the picosecond scale. The outer-well levels are much more weakly predissociated. We have estimated their widths (black dots in Fig. 13) using Fermi's golden rule together with the *ab initio* vibronic coupling function from Ref. 27. The agreement between experiment and theory is very satisfactory.

V. CONCLUSION

We have measured the absolute transition probabilities of the P(1) transitions arising in the photoabsorption $np\sigma\ ^1\Sigma_u^+, v \leftarrow X^1\Sigma_g^+, v'' = 0$ in H_2. The measurements cover the full vibrational progression v for the lower Rydberg states $4 \le n \le 9$. For higher-n Rydberg states (n up to 28) only the lower portion $0 \le v \le 3$ of the vibrational progression has been observed. Thirty one new P(1) lines have been assigned or reassigned.

The observations have been interpreted theoretically by MQDT, under the assumption that up to moderate R-values the excited electronic states are correctly described as $np\sigma$ Rydberg states associated with the vibrating /rotating $(v^+, N^+ = 1)$ ground state H_2^+ ion. It has been known for a long time that these levels exhibit strong non-adiabatic coupling;[5,10] here we have extended the previous analyses and studied the effect of the interactions on the line intensities. The strong vibronic interaction also causes fast

vibrational autoionization to occur. We have found that all $N = 0$ $np\sigma$, v levels corresponding to $n \geq 5$ and $v > 0$ are fully ionized, with no chance left for molecular dissociation and/or fluorescence to enter into competition.

The MQDT approach reproduces those observed levels which are confined to small R-values very well (≤ 1 cm^{-1}). These are the levels that do not extend into the non-Rydberg outer potential well of the $n = 4$ $B''\bar{B}$ state. Above the potential barrier the MQDT approach becomes problematic in as much as levels associated with the $B''\bar{B}$ state are concerned. The inclusion of the outer potential well of the $B''\bar{B}$ in the present analysis via the effective quantum defect curves of Fig. 1(c) is somewhat artificial from a physical point of view. An additional complication arises because near $R \approx 5.5$ a.u. the $n = 4$ and $n = 5$ $^1\Sigma_u^+$ state exhibit an avoided crossing arising from $p \sim f$ mixing. The outer portion of the $n = 5$ $^1\Sigma_u^+$ state therefore corresponds in essence to $4p\sigma$, whereas the outer portion of $n = 4$ does not. In this work, we have used non-crossing potential energy curves for the determination of the clamped-nuclei quantum defects and not attempted to treat the $p \sim f$ mixing explicitly. Nevertheless our results show that higher-n $np\sigma$, $N = 0$ levels are quite satisfactorily reproduced by MQDT, in particular also those levels for which no quantum-chemical potential energy curves exist and which are predicted on the basis of the quantum defects determined here.

Future developments of MQDT should include a unified treatment of long-range r/short-range R Rydberg states (where r stands for the electron-ion core distance) on the one hand, and short-range r/long-range R non-Rydberg states, of which the outer well of the $B''\bar{B}$ is an example. This second type of state can be viewed as a "heavy" Rydberg state[31] where the "core" is a H^- atom and the "outer" particle is a proton instead of an electron. This type of theoretical description has been pioneered recently by Kirrander.[32] Theoretical work aiming at combining the two types of Rydberg states into a single "hybrid" theoretical description is underway in our group.

Finally, our measurements afford a striking manifestation of the $\Delta v = 1$ propensity rule[29,30] in vibrational autoionization, which itself is a particular example of an energy gap law (see Fig. 12 and the accompanying discussion in Sec. IV C). This phenomenon is important beyond molecular spectroscopy: the sudden increase of the autoionization width, by somewhat more than an order of magnitude as seen in Fig. 12, has its counterpart in the decrease, also by somewhat more than an order of magnitude, observed in the dissociative recombination (DR) of H_3^+ ions with slow electrons near the first excited vibrational ionization threshold of H_3^+.[33] It has been shown[34] that DR of H_3^+ (and, indeed, of other polyatomic ions[30]) is dominated by vibrational autoionization and is basically a $\Delta v = 1$ vibrational electron capture process.

ACKNOWLEDGMENTS

We acknowledge the Helmholtz-Zentrum Berlin-Electron storage ring BESSY II for provision of synchrotron radiation at beamline U125/2-10m-NIM. M.G.-M. would like to thank Gerd Reichardt and Andreas Balzer for technical assistance. The research leading to these results has received funding from the European Community's Seventh Framework Programme (FP7/2007-2013) under grant agreement No. 226716. Ch.J. thanks the Miescher Foundation (Basel, Switzerland) for partial support. Ch.J. was further supported by the ANR (France) under contract 09-BLAN-020901. I.H. thanks the Deutsche Forschungsgemeinschaft (DFG) for funding. A.K. acknowledges the Otto-Braun-Fonds of the University of Kassel for funding. We are grateful to Dr. A. Kirrander and Dr. Z. S. Mezei (Orsay) for useful suggestions and help.

[1] A. L. Broadfoot, M. J. S. Belton, P. Z. Takacs, B. R. Sandel, D. E. Shemansky, J. B. Holberg, J. M. Ajello, S. K. Atreya, T. M. Donahue, H. W. Moos, J. L. Bertaux, J. E. Blamont, D. F. Strobel, J. C. McConnell, A. Dalgarno, R. Goody, and M. B. McElroy, Science **204**, 979 (1979).
[2] J. T. Clarke, H. W. Moos, S. K. Atreya, and A. L. Lane, Astrophys. J. **241**, 179 (1980).
[3] X. Liu, D. E. Shemansky, J. M. Ajello, D. L. Hansen, C. Jonin, and G. K. Hansen, Astrophys. J., Suppl. Ser. **129**, 267 (2000).
[4] U. Fano, Phys. Rev. A **2**, 353 (1970).
[5] G. Herzberg and Ch. Jungen, J. Mol. Spectrosc. **41**, 425 (1972).
[6] *Molecular Applications of Quantum Defect Theory*, edited by Ch. Jungen (The Institute of Physics, Bristol, 1996).
[7] M. Glass-Maujean and Ch. Jungen, J. Phys. Chem. **A 113**, 13124 (2009).
[8] M. Glass-Maujean, Ch. Jungen, H. Schmoranzer, A. Knie, I. Haar, R. Hentges, W. Kielich, K. Jänkälä, and A. Ehresmann, Phys. Rev. Lett. **104**, 183002 (2010).
[9] M. Glass-Maujean, Ch. Jungen, G. Reichardt, A. Balzer, H. Schmoranzer, A. Ehresmann, I. Haar, and P. Reiss, Phys. Rev. A **82**, 062511 (2010).
[10] Ch. Jungen and O. Atabek, J. Chem. Phys. **66**, 5584 (1977).
[11] P. M. Dehmer and W. A. Chupka, J. Chem. Phys. **65**, 2243 (1976).
[12] M. Glass-Maujean, S. Klumpp, L. Werner, A. Ehresmann, and H. Schmoranzer, J. Chem. Phys. **126**, 144303 (2007).
[13] M. Glass-Maujean, S. Klumpp, L. Werner, A. Ehresmann, and H. Schmoranzer, Mol. Phys. **105**, 1535 (2007).
[14] M. Glass-Maujean, S. Klumpp, L. Werner, A. Ehresmann, and H. Schmoranzer, J. Mol. Spectrosc. **249**, 51 (2008).
[15] M. Glass-Maujean, S. Klumpp, L. Werner, A. Ehresmann, and H. Schmoranzer, J. Chem. Phys. **128**, 094312 (2008).
[16] G. Staszewska and L. Wolniewicz, J. Mol. Spectrosc. **212**, 208 (2002); see also http://www.fizyka.umk.pl/ftp/publications/ifiz/luwo.
[17] G. Staszewska and L. Wolniewicz, J. Mol. Spectrosc. **217**, 181 (2003); see also http://www.fizyka.umk.pl/ftp/publications/ifiz/luwo.
[18] G. Reichardt, J. Bahrdt, J.-S. Schmidt, W. Gudat, A. Ehresmann, R. Müller-Albrecht, H. Molter, H. Schmoranzer, M. Martins, N. Schwentner, and S. Sasaki, Nucl. Instrum. Methods Phys. Res. A **467–468**, 462 (2001).
[19] C. H. Greene and Ch. Jungen, Adv. At. Mol. Phys. **21**, 51 (1985).
[20] K. P. Huber and G. Herzberg, *Constants of Diatomic Molecules* (Van Nostrand, Reinhold, New York, 1979).
[21] *The Hydrogen Molecule Wavelength Tables of Gerhard Heinrich Dieke*, edited by H. M. Crosswhite (Wiley, New York, 1972).
[22] H. Gao, Ch. Jungen, and C. H. Greene, Phys. Rev. A **47**, 4877 (1993).
[23] A. Matzkin, Ch. Jungen, and S. C. Ross, Phys. Rev. A **62**, 062511 (2000).
[24] T. Namioka, J. Chem. Phys. **40**, 3154 (1964); **41**, 2141 (1964).
[25] S. Takezawa, J. Chem. Phys. **52**, 2575 (1970).
[26] Ch. Jungen, S. T. Pratt, and S. C. Ross, J. Phys. Chem. **99**, 1700 (1995).
[27] L. Wolniewicz, T. Orlikowski, and G. Staszewska, J. Mol. Spectrosc. **238**, 118 (2006).
[28] Ch. Jungen and M. Raoult, Faraday Discuss Chem. Soc. **71**, 253 (1981).
[29] R. S. Berry, J. Chem. Phys. **45**, 1228 (1966).
[30] Ch. Jungen and S. T. Pratt, J. Chem. Phys. **133**, 214303 (2010).
[31] M. O. Vieitez, T. I. Ivanov, E. Reinhold, C. A. de Lange, and W. Ubachs, Phys. Rev. Lett. **101**, 163001 (2008).
[32] A. Kirrander, J. Chem. Phys. **133**, 121103 (2010).
[33] B. J. McCall, A. J. Huneycutt, R. J. Saykally, N. Djuric, G. H. Dunn, J. Semaniak, O. Novotny, A. Al-Khalili, A. Ehlerding, F. Hellberg, S. Kalhori, A. Neau, R. D. Thomas, A. Paal, F. Österdahl, and M. Larsson, Phys. Rev. A **70**, 052716 (2004).
[34] Ch. Jungen and S. T. Pratt, Phys. Rev. Lett. **102**, 023201 (2009).